Chemical Communication

COMMUNICATION

Cage-like MnO_2-Mn_2O_3 hollow spheres with high specific capacitance and high rate capability as supercapacitor material

Received 00th January 20xx,
Accepted 00th January 20xx

DOI: 10.1039/x0xx00000x

www.rsc.org/

Rongfang Wang,*[a] Yuanyuan Ma,[a] Hui Wang,[a] Julian Key,[b] Dan Brett,[c] and Shan Ji*[c]

Carbonaceous spheres were first prepared hydrothermally as templates for a subsequent hydrothermal step of MnO_2 shell precipitation. Following calcination to remove carbon, thinner shells resulted in cage-like MnO_2-Mn_2O_3 hollow spheres with high specific capacitance and high rate capability as supercapacitor material.

The development of active materials for aqueous electrolyte-based supercapacitors has attracted much research interest in recent years. Aqueous cell formats offer the advantages of lower material/construction costs and are less toxic than their organic electrolyte counterparts. However, due to the low cell voltage of aqueous systems, their active material must reach higher values of both specific capacitance (F g^{-1}) and rate performance (F g^{-1} at high current density A g^{-1}) to be competitive[1]. Hollow-structured electrode materials improve these properties due to their large surface area, high porosity, and shell permeability[2-4]. Furthermore, different synthesis strategies have managed to achieve hollow spheres[5-7], cubes[8], polyhedrons[2] and bowls[9], and their manipulation into double-layer shells[10, 11] and multi-layer shells[12, 13]. Hollow-nanostructured manganese oxides are attractive due to the high abundance, environmental friendliness and high theoretical specific capacity of manganese oxides [2, 14-17]. Various studies have reported hollow MnO_2 structures such as spheres[14-16, 18], tubes[19], urchin[20], and paramecium[21], prepared using methods employing oxidation-etching and hard-templates. These hollow-structured MnO_2 crystals have a specific capacitance range of ~100 to 300 F g^{-1} at current densities lower than 2 A g^{-1}. For example, Zhang and co-workers reported high specific capacitance of 210.2 F g^{-1} at 0.2 A g^{-1} in double-shelled MnO_2 hollow spheres synthesized via a self-templating route[22]. In such works, the shells usually form a completely continuous layer. However, hollow material with a cage-like shell (illustrated in Fig. 1) would perceivably provide an even larger material surface area, and also provide channels for rapid electrolyte ion movement. This would thus improve the material's performance in both supercapacitor and catalyst applications [23-25]. In other reports, hybridizing different phases of manganese oxides has resulted in increased overall specific capacitance. For instance, Mn_2O_3-Mn_3O_4 fibers of 360.7 F g^{-1} at 1 A g^{-1} produced higher specific capacitance than that of either respective single phase due to a proposed reduced interfacial resistance of the mixed-phase manganese oxides[26]. Similarly, manganese oxide hybrids, Mn_2O_3-Mn_3O_4[27, 28], MnO-Mn_3O_4[29], have also produced enhanced electrode performance as supercapacitor material, and on this basis other manganese oxides hybrids are also clearly worth exploring.

In the present study, cage-like MnO_2-Mn_2O_3 hollow spheres (CMHS) were prepared using a carbon template method. Carbonaceous (C) spheres were chosen as the removable template, as has been used in other studies to produce hollow materials such as TiO_2[30], Mn_2O_3[31] and MnO_2[17]. The C spheres have the advantages of ease of large-scale preparation, good dispersion in solvents, and easy removal by calcination in air. Herein, it was found that by reducing the concentration of Mn precursor in combination with reducing hydrothermal dwell time, cage-like mixed phase MnO_2-Mn_2O_3 hollow spheres (CMHS) could be produced. Interestingly, the Mn_2O_3 phase was practically absent in the MnO_2 hollow spheres (MHS), suggesting that reduction via carbon to form Mn_2O_3 was lessened in higher concentrations of manganese precursor. The CMHS particles produced higher specific capacitance than MHS and had correspondingly higher rate capability, suggesting that both hybrid composition and cage-like structure accounted for this improvement.

Fig. 1 shows the strategy for synthesizing uniform cage-like MnO_2-Mn_2O_3 hollow spheres (CMHS) and MnO_2 hollow spheres (MHS). Firstly, C spheres (SEM image provided in Fig. S1) are synthesized hydrothermally, followed by a second hydrothermal treatment in the presence of $KMnO_4$ to form C@MnO_2 core/shell structures, followed

[a] College of Chemistry and Chemical Engineering, Northwest Normal University, Lanzhou, 730070, China, E-mail: wangrf@nwnu.edu.cn
[b] South African Institute for Advanced Materials Chemistry, University of the Western Cape, Bellville, Cape Town 7535, South Africa
[c] Dept. Chemical Engineering, University College London, London WC1E 7JE, UK, E-mail: shan.ji@ucl.ac.uk

† Electronic Supplementary Information (ESI) available: Experiential details, SEM and TEM images of carbonaceous spheres and C/Mn_2O_3, XRD pattern, N_2 isotherms, CV curves, charge/discharge curves and cycling performance. See DOI: 10.1039/x0xx00000x

by their calcination in air to remove the carbon by oxidation. CMHS (Fig. 2) was formed by reducing the concentration of Mn precursor in combination with reducing hydrothermal dwell time.

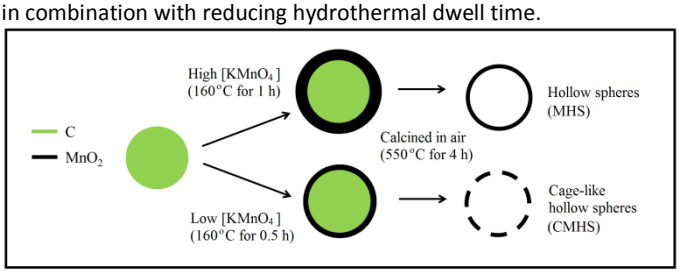

Fig. 1 Synthesis route of hollow manganese oxide shells and cage-like shells

Fig. S2 shows the morphology of the CMHS core/shell precursors, C@MnO_2-1, which appear as spheres with smooth outer surfaces (as prepared by hydrothermal reaction). Their diameters ranged between 400 to 800 nm due to size variation of the C spheres. Transmission electron microscopy (TEM) in Fig. S2c shows the visible contrast between shell and core, with high-resolution TEM (HRTEM) in Fig. S2d showing the shell thickness to be ~80 nm. The core-shell structure was also confirmed by the overlapped elemental mapping of C, Mn, and O image (Fig. S2f-m). Powder X-ray diffraction (XRD) analysis (Fig. S3), shows the phase of C@MnO_2 indexed to monoclinic δ-MnO_2 (JCPDS PDF 43-1456). After calcination, the uniform spherical morphology for CMHS was perfectly retained (Fig. 2a), and the cage-like surface of CMHS is clearly shown in the magnified SEM images (Fig. 2b). The typical diameter of CMHS decreases slightly to ~400–600 nm. This could be due to a contraction effect caused by the decomposition of C spheres at elevated temperature[30]. The cage-like surface and hollow center of CMHS is clearly shown in the TEM image (Fig. 2c). The magnified TEM image in Fig. 2d shows that the surface of CMHS was composed of connected nanocrystals. HRTEM (Fig. 2e) shows the microstructure of the nanocrystals had clear lattice fringes, indicating the product was highly crystalline after calcination. The interplanar distance between the lattice fringes measured 0.21 nm, which indexes to (420) crystal planes of cubic Mn_2O_3. Powder X-ray diffraction (XRD) analysis (Fig. 2F) shows the phase of CMHS indexed to the tetragonal α-MnO_2 (JCPDS PDF 72-1982) and cubic Mn_2O_3 (JCPDS PDF 41-1442). Therefore, CMHS is a mixed phased hybrid of α-MnO_2 and Mn_2O_3. The transformation of δ-MnO_2 into Mn_2O_3 is likely to have occured via reduction of δ-MnO_2 by carbon. Brunauer–Emmett–Teller (BET) analysis of CMHS (Fig. S4) shows it had a relatively high specific surface area of 54.2 $m^2 g^{-1}$.

For comparison, MHS (with a complete shell) was also characterized. The surface of the MHS precursor, C@MnO_2-2, (Fig. S5a and b) comprised connected MnO_2 nanoflakes ranging from 0.5-1 µm. TEM (Fig. S5c,d) shows the rough surface of C@MnO_2-2 core/shell spheres and the thickness of the shell to be ~150 nm. The core-shell structure of the C@MnO_2-2 spheres is also confirmed by the overlapped elemental mapping of C, Mn, and O image (Fig. S5 e-i). Compared to C@MnO_2-1, the thickness of the shell for C@MnO_2-2 was considerable larger. After calcination, the spherical morphology was perfectly retained in the resultant MHS (Fig. 3a), and the surface of the spheres remained composed of

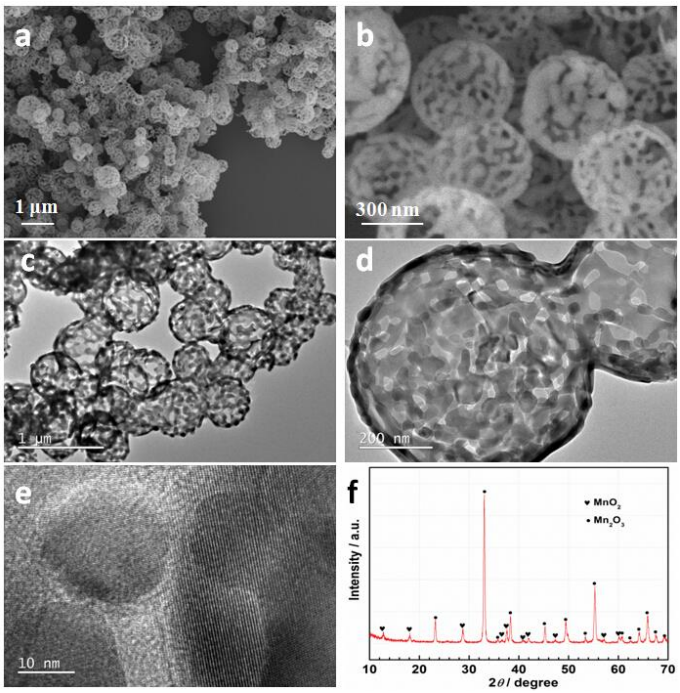

Fig. 2 Physical characterization of CMHS: (a, b) SEM; (c-e) TEM; and (f) XRD.

well connected nanoparticles (Fig. 3b). The hollow center of the annealed product is clearly shown through the TEM images (Fig. S3c and d) and the shell thickness was ~70 nm with a relatively rough outer surface. The typical diameter of MnO_2 hollow spheres ranged between ~500-800 nm, and was larger than that of CHMS (~400-600 nm). The XRD pattern (Fig. S6), again indexed to tetragonal α-MnO_2 (JCPDS PDF 72-1982) and cubic Mn_2O_3 (JCPDS PDF 41-1442). However, compared to the CMHS XRD pattern, the intensity of the cubic Mn_2O_3 peaks were considerably reduced, likey resulting from the higher loading of MnO_2 relative to the amount of carbon. The BET specific surface area of MHS was 34.1 $m^2 g^{-1}$ (Fig. S7) and less than that of CHMS (54.2 $m^2 g^{-1}$).

The electrochemical performance of CHMS and MHS was evaluated by cyclic voltammetry (CV) and galvanostatic charge–discharge cycling in three-electrode cells containing 0.5 mol L^{-1} Na_2SO_4 electrolyte. Fig. 4a shows CV curves of the CMHS electrodes carried out over potential range of -0.654 ~ 0.146 V *vs.* Hg/Hg_2SO_4 at scan rates of 1, 2, 5, 10, 20, 50 and 100 mV s^{-1}. The CV plots all occurred as approximately symmetric rectangles without any apparent redox peaks, and were therefore indicative of capacitive charge/discharging [32, 33]. At high scan rates from 10 to 100 mV s^{-1}, the CV curves show distortion from rectangular shape owing to electrode polarization. The charge mechanism of manganese oxides in electrolytes containing alkaline metal cations (A^+) is shown below, where transition between Mn^{3+} and Mn^{4+} occurs at surface sites accessible to electrolyte ions [34].

$MnO_2 + A^+ + e^- \leftrightarrow MnOOA^+$

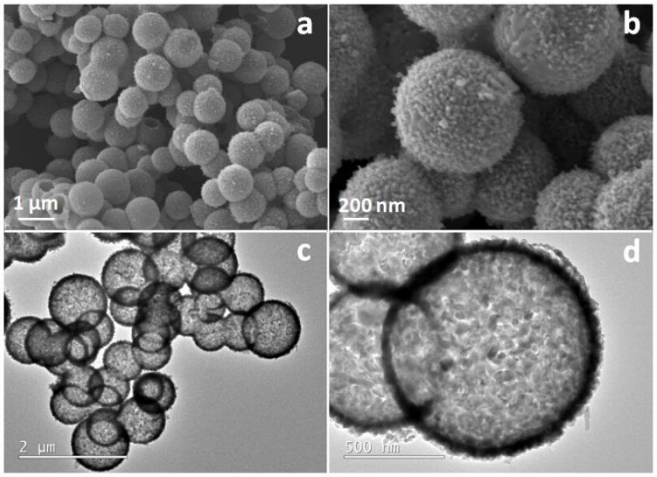

Fig. 3 Physical characterization of MHS: (a, b) SEM; and (c, d) TEM.

Capacitance via the above mechanism at high scan rates or high current densities is thought to only occur within a thin surface layer of manganese oxides [35]. However, at very low scan rates, A^+ ions may also intercalate deeper into the material structure, which can raise the observed specific capacitance. At high scan rates electrode polarization typically lowers the available specific capacitance [36]. Fig. 4b shows the specific capacitance ($C_{sp,CV}$, F g^{-1}) values of CMHS at different scan rates calculated from the CV plots (note: CV plots for MHS are shown Fig. S8). For both CHMS and MHS, increasing scan rates decreased the specific capacitance due to limitations in the Na^+ diffusion rate [14]. At a scan rate of 1 mV s^{-1}, CMHS and MHS produced $C_{sp,CV}$ specific capacitances of 239.8 F g^{-1} and 178.3 F g^{-1} respectively. The higher CMHS value coincides with its higher BET value, which is in accordance with theory [37-40]. In addition, the specific balance of mixed phases in CMHS may be another factor contributing to its higher observed specific capacitance, resulting from possibly improved surface conductivity [26-29].

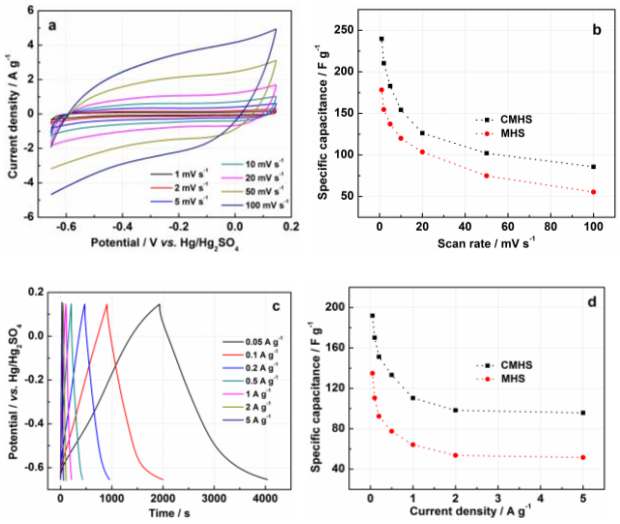

Fig. 4. (a) CV curves of the CMHS at scan rate of 1, 2, 5, 10, 20, 50 and 100 mV s^{-1}; (b) specific capacitance as calculated from CV for CMHS and MHS; (c) galvanostatic charge-discharge curves of CMHS at 0.5 to 5 A g^{-1}; and (d) rate capability of CMHS and MHS.

To determine the electrochemical performance of CMHS and MHS under galvanostatic cycling conditions, cycling was carried out over a 0.05 A g^{-1} to 5 A g^{-1} current range (Fig. 4c and Fig. S9). At a current density of 0.05 A g^{-1}, the respective discharge specific capacitances ($C_{sp,Dis}$) of CMHS and MHS were 191.9 F g^{-1} and 134.9 F g^{-1}. This pattern matched that of the CV results, and in comparison with previous reports on hollow-structured manganese oxides, the specific capacitance for CMHS produced via CV and galvanostatic cycling are quite competitive. Previously reported values include: hollow MnO_2 spheres of 115 F g^{-1} at 0.5 A g^{-1} in 1 M Na_2SO_4 electrolyte [14]; double-shelled MnO_2 hollow spheres of 210.2 F g^{-1} at 0.2 A g^{-1} in 1 M Na_2SO_4 electrolyte [22]; hollow α-MnO_2 of 167 F g^{-1} at 2.5 mA cm^{-2} in 1 M Na_2SO_4 electrolyte [18]; and nano-structured MnO_2 hollow spheres of 147 F g^{-1} at 0.2 A g^{-1} in 1-butyl-3-methylimidazolium hexaurophosphate in DMF electrolyte [41]. However, MnO_2 hollow paramecium of 554.3 F g^{-1} at 1 A g^{-1} [21] and hollow tubular MnO_2 of 315 F g^{-1} at 0.2 A g^{-1} [19] are the exceptionally high examples in the field.

Fig. 4d shows the $C_{sp,Dis}$ of both CMHS and MHS gradually decreased with increasing current density, which matches previous literature on MnO_2 electrodes[17, 39, 42]. Increasing current density thus decreases mass efficiency/utilization. As current density was increased from 0.05 A g^{-1} to 5 A g^{-1} (Fig. 4d), CMHS and MHS retained 49.9% and 38.3% of their initial specific capacitance respectively, i.e. with CMHS decreasing from 191.9 F g^{-1} to 95.7 F g^{-1}, and MHS decreasing from 134.9 F g^{-1} to 51.6 F g^{-1}. Therefore, the higher rate capability of CMHS suggests its open cage-like structure facilitates faster electrolyte ion movement to and from its accessible surface area.

Long-term cycling stability of electrode material is an important factor for practical applications. Fig. S10 shows the specific capacitance retention of CMHS and MHS after 2000 charge-discharge galvanostatic cycles at 2 A g^{-1} were 77.4% and 68.2% respectively. The high cycling stability of CMHS is comparable to that of various reported MnO_2-based electrodes[33, 35, 42] such as carbon@MnO_2 core-shell spheres [33] and mesoporous MnO_2/polyaniline hollow spheres[42], but lower than hollow MnO_2 tubes[19] and nano-structured MnO_2 hollow spheres in 1-butyl-3-methylimidazolium hexaurophosphate in DMF electrolyte [41]. However, in our case it was found that the electrolyte did slightly discolour after 2000 cycles. This indicates the dissolution of the MnO_2 to soluble Mn^{2+} at low potentials, which is a main cause of capacitance loss in MnO_2-based supercapacitors[43]. This may suggest that CMHS and MHS are less stable than other forms of MnO_2 at low potentials (a possibility we are currently investigating). Overall, however, the improved specific capacitance, rate capability, and long-term capacity retention of the cage like particles offers a promising target structure for future research.

In summary, cage-like MnO_2–Mn_2O_3 hollow spheres (CHMS) were successfully prepared using hydrothermal synthesis on carbon sphere templates, followed by template removal via calcination. Mn precursor concentration and hydrothermal dwell time were tuneable to produce CHMS or complete shell structure (MHS – manganese oxide hollow spheres). Cage-like structure resulted from reduced thickness of the MnO_2 shell of the CMHS precursor, which also increased the amount of Mn_2O_3 to MnO_2 content after carbon template removal, possibly through greater reduction of MnO_2 by carbon. The BET surface area of CMHS, owing to its cage-like

structure, was ~37% larger than that of MHS. At a CV scan rate of 1 mV s^{-1} the specific capacitance of CMHS and MHS were 239.8 F g^{-1} and 178.3 F g^{-1} respectively. With a current density increase from 0.05 A g^{-1} to 5 A g^{-1}, CMHS and MHS retained 49.9% and 38.3% of their initial specific capacitance. After 2000 cycles at 2 A g^{-1}, CMHS and MHS retained 77.4% and 68.2% of their initial specific capacitance. Therefore, CMHS had improved specific capacitance, rate capability, and long-term capacity retention. These properties correlate to the higher available surface area and greater macro-porosity of CMHS. Cage-like particles thus offer a promising target structure for supercapacitor material, and adjusting precipitate coating thickness offers a simple approach for their synthesis.

Notes and references

1 W. Wei, X. Cui, W. Chen and D. G. Ivey, *Chemical Society reviews*, 2011, **40**, 1697-1721.
2 M. Fang, X. Tan, M. Liu, S. Kang, X. Hu and L. Zhang, *CrystEngComm*, 2011, **13**, 4915.
3 Y. Zhang, Q.-q. Yao, H.-l. Gao, L.-x. Wang, L.-z. Wang, A.-q. Zhang, Y.-h. Song and T.-c. Xia, *Powder Technology*, 2014, **267**, 268-272.
4 Z. Ma, X. Yuan, L. Li, Z.-F. Ma, L. Zhang, L. Mai and J. Zhang, *Journal of Power Sources*, 2015, **291**, 156-162.
5 B. C. Sekhar and N. Kalaiselvi, *CrystEngComm*, 2015, **17**, 5038-5045.
6 R. Liu, S. Zhao, M. Zhang, F. Feng and Q. Shen, *Chem. Comm.*, 2015, **51**, 5728-5731.
7 H. Qian, G. Lin, Y. Zhang, P. Gunawan and R. Xu, *Nanotechnology*, 2007, **18**, 355602.
8 L. Liu, X. Zhang, R. Wang and J. Liu, *Superlattices and Microstructures*, 2014, **72**, 219-229.
9 J. Liang, X. Y. Yu, H. Zhou, H. B. Wu, S. Ding and X. W. Lou, *Angew Chem Int Ed Engl*, 2014, **53**, 12803-12807.
10 Y. Qiao, Y. Yu, Y. Jin, Y.-B. Guan and C.-H. Chen, *Electrochimica Acta*, 2014, **132**, 323-331.
11 W.-h. Lee and J. H. Moon, *ACS Applied Materials & Interfaces*, 2014, **6**, 13968-13976.
12 G. Zhang and X. W. Lou, *Angew Chem Int Ed Engl*, 2014, **53**, 9041-9044.
13 X. Lai, J. Li, B. A. Korgel, Z. Dong, Z. Li, F. Su, J. Du and D. Wang, *Angew Chem Int Ed Engl*, 2011, **50**, 2738-2741.
14 D. Han, X. Jing, P. Xu, Y. Ding and J. Liu, *Journal of Solid State Chemistry*, 2014, **218**, 178-183.
15 X. Tang, Z.-h. Liu, C. Zhang, Z. Yang and Z. Wang, *Journal of Power Sources*, 2009, **193**, 939-943.
16 S. Maiti, A. Pramanik and S. Mahanty, *RSC Advances*, 2015, **5**, 41617-41626.
17 J. Yue, X. Gu, L. Chen, N. Wang, X. Jiang, H. Xu, J. Yang and Y. Qian, *Journal of Materials Chemistry A*, 2014, **2**, 17424-17426.
18 M. Xu, L. Kong, W. Zhou and H. Li, *The Journal of Physical Chemistry C* 2007, **111**, 19141-19147.
19 J. Zhu, W. Shi, N. Xiao, X. Rui, H. Tan, X. Lu, H. H. Hng, J. Ma and Q. Yan, *ACS applied materials & interfaces*, 2012, **4**, 2769-2774.
20 X. Feng, Z. Yan and N. Chen, *Chinese Journal of Inorganic Chemistry*, 2014, **30**, 2509-2515.
21 Z. Wen, W. She, Y. Li and R. Che, *Journal of Materials Chemistry A*, 2014, **2**, 20729-20738.
22 X.-y. Zhang, L.-q. Han, C.-y. Wang and M.-m. Chen, *Materials Letters*, 2014, **136**, 78-80.
23 M. H. Oh, T. Yu, S.-H. Yu, B. Lim, K.-T. Ko, M.-G. Willinger, D.-H. Seo, B. H. Kim, M. G. Cho, J.-H. Park, K. Kang, Y.-E. Sung, N. Pinna and T. Hyeon, *Science*, 2013, **340**, 964-968.
24 Y. Sui, W. Fu, Y. Zeng, H. Yang, Y. Zhang, H. Chen, Y. Li, M. Li and G. Zou, *Angewandte Chemie International Edition*, 2010, **49**, 4282-4285.
25 Y. Wang, L. Zhang, Y. Wu, Y. Zhong, Y. Hu and X. W. Lou, *Chemical Communications*, 2015, **51**, 6921-6924.
26 E. Lee, T. Lee and B.-S. Kim, *Journal of Power Sources*, 2014, **255**, 335-340.
27 A. T. Chidembo, S. H. Aboutalebi, K. Konstantinov, C. J. Jafta, H. K. Liu and K. I. Ozoemena, *RSC Adv.*, 2014, **4**, 886-892.
28 C.-K. Lin, K.-H. Chuang, C.-Y. Lin, C.-Y. Tsay and C.-Y. Chen, *Surface and Coatings Technology*, 2007, **202**, 1272-1276.
29 Y. Du, X. Zhao, Z. Huang, Y. Li and Q. Zhang, *RSC Advance*, 2014, **4**, 39087-39094.
30 G. Zhang, H. B. Wu, T. Song, U. Paik and X. W. Lou, *Angew Chem Int Ed Engl*, 2014, **53**, 12590-12593.
31 C. Cheng, Y. Huang, N. Wang, T. Jiang, S. Hu, B. Zheng, H. Yuan and D. Xiao, *ACS Applied Materials & Interfaces*, 2015, **7**, 9526-9533.
32 J. Sodtipinta, W. Pon-On, W. Veerasai, S. M. Smith and P. Pakawatpanurut, *Materials Research Bulletin*, 2013, **48**, 1204-1212.
33 Y. Zhao, Y. Meng and P. Jiang, *Journal of Power Sources*, 2014, **259**, 219-226.
34 S. C. Pang, M. A. Anderson and T. W. Chapman, *Journal of The Electrochemical Society*, 2000, **147**, 444-450.
35 R. Jiang, T. Huang, J. Liu, J. Zhuang and A. Yu, *Electrochimica Acta*, 2009, **54**, 3047-3052.
36 Q. Qu, P. Zhang, B. Wang, Y. Chen, S. Tian, Y. Wu and R. Holze, *The Journal of Physical Chemistry C*, 2009, **113**, 14020-14027.
37 L.-L. Yu, J.-J. Zhu and J.-T. Zhao, *Journal of Materials Chemistry A*, 2014, **2**, 9353.
38 G. Wang, L. Zhang and J. Zhang, *Chemical Society reviews*, 2012, **41**, 797-828.
39 S. Devaraj and N. Munichandraiah, *The Journal of Physical Chemistry C*, 2008, **112**, 4406-4417.
40 P. Ragupathy, D. H. Park, G. Campet, H. N. Vasan, S.-J. Hwang, J.-H. Choy and N. Munichandraiah, *The Journal of Physical Chemistry C*, 2009, **113**, 6303-6309.
41 S. Maiti, A. Pramanikab and S. Mahanty, *RSC Advance*, 2015, **5**, 41617-41626.
42 J.-G. Wang, Y. Yang, Z.-H. Huang and F. Kang, *Journal of Power Sources*, 2012, **204**, 236-243.
43 J. Yan, E. Khoo, A. Sumboja and P. S. Lee, *ACS Nano*, 2010, **4**, 4247-4255.

